Chapter 2

Hyperpolarized Gas Production and Polarimetry

2.1 Background

Optical pumping of alkali-metal atoms was introduced by Kastler [31] and Hawkins [32] at the beginning of the 1950s. Kastler received a Nobel Prize for the discovery and the development of optical methods for studying Hertzian resonances in atoms in 1966. Dehmelt [33] used optical pumping to study T_1 relaxation of polarized sodium atoms. The first published study of spin transfer (then called "dipolar-exchange") from the alkali-metal to ^{3}He was done by Bouchiat *et al.* [34] in 1960, and was extended to include all stable noble gas isotopes by Grover [35] in 1978. In the seventies and eighties, Happer *et al.* published several papers [1, 36, 17, 37] which laid out the theoretical foundations for hyperpolarized gas production using optical pumping and spin-exchange techniques. But it was not until the nineties, when researchers realized the potential of hyperpolarized gases for a wide range of applications, that the field really started to grow.

In the last ten years, hyperpolarized ^{3}He has been used as a target in nuclear physics experiments [14], and as an MR imaging agent for MR ventilation studies of animal and human lungs [38, 39]. Hyperpolarized ^{129}Xe has been used in MR imaging of materials [40] as well as in MR imaging of blood [41, 42] and animal brain [43]. In addition, the production [44, 45] and storage [46] of hyperpolarized gases have been optimized greatly and continue to improve.[1]

The polarization levels of noble gases have primarily been measured using the MR tech-

[1] In addition to polarization by spin-exchange with optically polarized alkali-metal, ^{3}He can also be polarized using direct optical pumping of its metastable $2\,^3S_1$ state [47].

nique of Adiabatic Fast Passage (AFP) [48]. However, the NMR-AFP polarimetry requires calibration against a source of known thermal polarization, usually water. In 1989, Schaefer *et al.* [5] introduced an absolute polarimetry technique based on the frequency shift of the electron paramagnetic resonance (EPR) of the alkali-metal. Since then, EPR polarimetry was implemented successfully for measuring polarization of ^{3}He during experiments at the Thomas Jefferson Laboratory in Virginia [49, 50, 51, 52], and at the Stanford Linear Accelerator Center [53].

The precision of the EPR polarimetry depends on the calibration of the EPR frequency shift as a function of the noble gas magnetization. The calibration constant $\kappa_\circ$ has been measured for Rb-^{3}He by Newbury *et al.* [4], and to a greater accuracy by Romalis *et al.* [3]. However, a comparable measurement of $\kappa_\circ$ for Rb-^{129}Xe interaction is still needed for ^{129}Xe EPR polarimetry to be used.

One of the disadvantages of the EPR technique is that it can only be used for measuring the noble gas polarization in the presence of an alkali-metal and a laser beam. As such, it is not suitable for *in vivo* polarimetry applications. Despite this limitation, the method is advantageous for a certain class of application, such as high-precision polarimetry required in hyperpolarized target experiments, or for applications requiring compact, cost-effective and reliable polarimetry setup.

2.2 Hyperpolarized Gas Production

Polarizing noble gases (either ^{129}Xe or ^{3}He) to achieve non-equilibrium polarization levels, which can be up to five orders of magnitude larger than the thermal polarization, is a two step process. First, the outer electron of an alkali-metal (usually, rubidium) is polarized using the technique of optical pumping with circularly polarized laser light tuned to the D1 spectral transition (7850 $\AA$) in rubidium. Second, the rubidium electron polarization is transferred to the nuclei of the noble gas during spin-exchange collisions via a Fermi contact interaction. We describe optical pumping and spin-exchange processes in the following two sections.

2.2.1 Optical Pumping

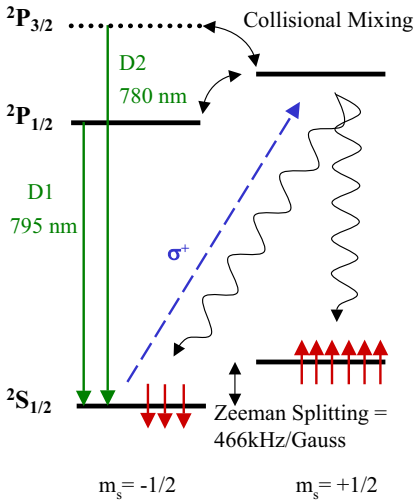

Figure 2.1: Electron levels in ^{85}Rb atom, assuming $I_{Rb} = 0$. The vertical axis is not drawn to scale.

A pictorial view of optical pumping is presented in Figure 2.1. For simplicity, the diagram ignores the rubidium nuclear spin. A more detailed view of the ^{85}Rb magnetic sublevels which takes into account the rubidium nuclear spin ($I = 5/2$ for ^{85}Rb, $I = 3/2$ for ^{87}Rb) is given in Figure 2.2.

When rubidium is placed in a magnetic field, the Zeeman sublevels ($m_S = \pm 1/2$) split. At low fields (20 G) the splitting is proportional to the magnetic field B, so that $\nu = \gamma_{Rb}\, B$, where $\gamma_{Rb} = 466$ kHz/G. Figure 2.1 shows the splitting of the $^2S_{1/2}$ ground level and the

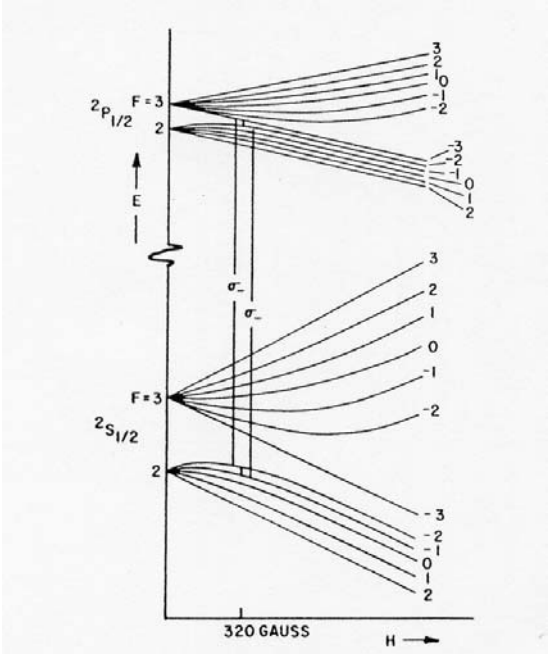

Figure 2.2: ^{85}Rb magnetic sublevels. Taken from a paper by W. Happer [1].

$^2P_{1/2}$ excited level. Initially, the difference in the electron populations between the two m_S sublevels is thermal in nature and thus small. However, a non-equilibrium polarization can be achieved by using circularly polarized light (with either positive or negative angular momentum) tuned to 7950 $\mathring{A}$ to excite selectively transitions from either ($^2S_{1/2},\ m_S = -1/2$) to ($^2P_{1/2},\ m_S = +1/2$) or from ($^2S_{1/2},\ m_S = +1/2$) to ($^2P_{1/2},\ m_S = -1/2$), but not both. Collisions with the noble gas atoms then rapidly equalize the populations of the excited state sublevels [19]. Normally, the electrons decay back to the ground level by emitting radiation at the D1 and D2 wavelengths.[2] Since this radiation is unpolarized, it would destroy the electron polarization by non-selectively exciting electron transitions from both Zeeman $^2S_{1/2}$ sublevels. To minimize the radiative decay back to the ground level, a buffer gas, such as nitrogen, is used. Electrons then transfer their energy to the rotational and vibrational modes of the nitrogen molecule [53] and decay to both ground-state sublevels with equal probability. Nitrogen densities of 0.1 amagats (approx. 0.1 atm) suffice to eliminate radiation trapping as a source of relaxation [1]. Continuous selective excitation of the electrons will depopulate one of the Zeeman sublevels and leave approximately 80% of electrons in the non-excitable Zeeman sublevel.

[2]The transition from $^2P_{1/2}$ level is called D1 transition, while the transition from $^2P_{3/2}$ level is called D2 transition. These transition will be mentioned again in the section on EPR polarimetry.

The Hamiltonian of the rubidium atom in a holding magnetic field $\mathbf{B} = B_\circ \hat{\mathbf{z}}$ is [19]

$$H = A_e \, \mathbf{I} \cdot \mathbf{S} + g_e \, \mu_B \, S_z \, B_z - \frac{\mu_I}{I} \, I_z \, B_z. \tag{2.1}$$

The first term in Eq. 2.1 represents the hyperfine interaction between the alkali-metal nuclear spin I ($I = 5/2$ for ^{85}Rb), and the electron spin S. The strength of this interaction is characterized by the isotropic magnetic-dipole coupling coefficient A_e. The second and third terms describe the coupling of the electron and nuclear spins with the magnetic field $\mathbf{B}$. The constant $g_e = 2.00232$ for the electron, μ_B is the Bohr magneton ($\mu_B = 9.2741 \times 10^{-21}$ erg G^{-1}), μ_I is the nuclear magnetic moment of the alkali-metal and I is the nuclear-spin quantum number. Since $\mu_B \gg \mu_I$, the Zeeman splitting is dominated by the electron spin. Furthermore, at low fields most commonly used for optical pumping applications (magnetic fields in the range of 1-30 G), the hyperfine interaction dominates over the Zeeman interactions, so the computations can be done in the eigenstates of the total angular momentum $\mathbf{F} = \mathbf{I} + \mathbf{S}$.

The local rubidium polarization P_{Rb} approaches a steady state. It is expressed in terms of the local mean optical pumping rate per unpolarized alkali-metal atom $\gamma_{opt}(\mathbf{r})$, and the electron spin destruction rate Γ_{SD} [18, 6]:

$$P_{Rb} = \frac{\gamma_{opt}(\mathbf{r})}{\gamma_{opt}(\mathbf{r}) + \Gamma_{SD}}. \tag{2.2}$$

The local mean optical pumping rate is

$$\gamma_{opt}(\mathrm{r}) = \int_0^\infty \Phi(\mathrm{r}, \nu) \, \sigma_{op}(\nu - \nu_\circ) \, d\nu, \tag{2.3}$$

where $\Phi(\mathrm{r}, \nu)$ is the laser intensity per unit frequency, while $\sigma_{op}(\nu - \nu_\circ)$ is the cross section for absorption of unpolarized light. The electron spin destruction rate is dominated by collisions of rubidium with other gas particles, rather than by the collisions with the glass walls of the cell. It can be expressed as [54]

$$\Gamma_{SD} = k_{Rb-NG} \, n_{NG} + k_{Rb-Rb} \, n_{Rb} + k_{Rb-N_2} \, n_{N_2}, \tag{2.4}$$

where the spin destruction rates $k_{Rb-x}[\mathrm{cm}^3/\mathrm{s}]$ have been measured by Wagshul *et al.* [55],

while the gas number densities n_x are a function of the cell composition. Rubidium number density n_{Rb} can be estimated from the Killian formula [4], $\log_{10} n_{Rb} = 26.41 - 4132/T - \log_{10} T$, where the Rb number density is in units of $1/\text{cm}^3$ and temperature is in units of K. In ^{129}Xe experiments, $T \approx 90°$ C, so $n_{Rb} \approx 3 \times 10^{12}$ cm^{-3}, while during ^{3}He experiments, $T \approx 140°$ C, so $n_{Rb} \approx 6 \times 10^{13}$ cm^{-3}.

2.2.2 Spin Exchange

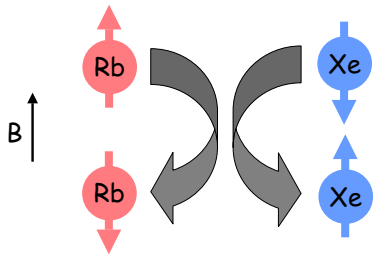

Figure 2.3: Spin transfer between the rubidium electron and the noble gas nucleus.

Spin exchange is the process by which the alkali-metal electrons transfer their polarization to the spin-1/2 nuclei of the noble gas (see Figure 2.3). The interaction Hamiltonian between ^{85}Rb and ^{129}Xe is [17]

$$H = \gamma \mathbf{N} \cdot \mathbf{S} + \alpha \mathbf{K} \cdot \mathbf{S}. \tag{2.5}$$

The first term in Eq. 2.5 is the spin-rotation interaction between the alkali-metal electron spin $\mathbf{S}$ and the rotational angular momentum $\mathbf{N}$ of the alkali-metal–noble-gas molecule. This term represents the loss of the alkali-metal electron polarization to the orbital angular momentum of the alkali-metal–noble-gas pair. The second term describes the isotropic hyperfine interaction (or so-called Fermi-contact interaction) responsible for the spin exchange between the alkali-metal electron spin $\mathbf{S}$ and the noble gas nuclear spin $\mathbf{K}$. γ and α are coupling coefficients which depend on the intermolecular separation and velocity of the unbound colliding pair [17].

The time evolution of the noble gas polarization can be approximated by an exponential equation, given as

$$P_{NG}(t) = \langle P_{Rb} \rangle \frac{\gamma_{SE}}{\gamma_{SE} + \Gamma} \left\{ 1 - e^{-(\gamma_{SE} + \Gamma)t} \right\}, \tag{2.6}$$

where $\langle P_{Rb} \rangle$ is the average rubidium polarization in the cell and can be determined from Eq. 2.2; Γ is the noble gas nuclear spin relaxation rate in the absence of Rb vapor; and $\gamma_{SE} = k_{SE}\, n_{Rb} = \langle v\sigma_{SE} \rangle\, n_{Rb}$ is the spin-exchange rate. The most recent measurement of the velocity averaged He-Rb spin-exchange cross section was done by Baranga *et al.* [56]: $k_{SE} = (6.7 \pm 0.6) \times 10^{-20}$ cm^3/s. Xe-Rb spin-exchange cross section is still being investigated as a result of two contradictory measurements: Cates *et al.* [57] measured $k_{SE} = (3.70 \pm 0.70) \times 10^{-16}$ cm^3/s, while Jau *et al.* [58] measured $k_{SE} = (1.72 \pm 0.08) \times 10^{-16}$ cm^3/s.

The noble gas nuclear spin relaxation rate in Eq. 2.6 is a function of the spin-relaxation resulting from the dipole interaction between the noble gas atoms, Γ_D; the spin-relaxation resulting from the collisions with the paramagnetic impurities in the walls of the cell, Γ_{Wall}; and the spin loss due to the magnetic field gradients, $\Gamma_{\Delta B}$ [53]:

$$\Gamma = \Gamma_D + \Gamma_{Wall} + \Gamma_{\Delta B}. \tag{2.7}$$

2.2.3 Experimental Setup

The experimental procedure consists of two main steps. After the cells are made at a glassblower shop, they are filled with a noble gas, nitrogen and an alkali-metal on our vacuum-gas system. The noble gas in the cells is then polarized using the optical pumping system.

2.2.3.1 Vacuum System and Cell Production

The noble gas used in our experiments is contained in sealed glass cells. In addition to ^{3}He (or ^{129}Xe), a few milligrams of Rb metal and a small amount of nitrogen gas were also introduced into the cells. Two cells were used in our experiments: a ^{3}He cell and a ^{129}Xe cell. The gas composition of these cells is given in Table 2.1. The cells had two cylindrical chambers and a tubing connecting the two chambers (see Figure 2.4). The top chamber was used for optical pumping and EPR polarimetry, while the bottom chamber was used for NMR polarimetry.[3] The dimensions and the shape of the cells are based on several requirements. First, the surface-to-volume ratio of the pumping chamber has to be minimized in order to decrease the surface relaxation rate of polarized gas nuclei per

[3]The two-chamber cell geometry was inherited from SLAC experiments, in which a laser beam was directed onto the top chamber to optically pump the gas, while an electron beam was directed onto the bottom chamber to study the spin structure of the neutron.

unit volume. This means that ideally, the pumping chamber would have to be spherical. However, laser beam reflects and refracts on a curved glass surface, potentially minimizing the efficiency of optical pumping. A cylindrically shaped cell, with nearly flat front and back optical windows is preferable.

	Hyp Gas Pressure (atm)	Nitrogen Pressure (atm)
^{129}Xe Cell	0.10	0.06
^{3}He Cell	8.36	0.08

Table 2.1: The gas content of ^{129}Xe and ^{3}He cells used at Caltech. All pressures measured at room temperature. ^{3}He cell parameters taken from [2].

The ^{3}He cell was filled by Hunter Middleton during his PhD research and was used in the E-142 experiment at SLAC which measured the spin structure of the neutron. A detailed description of cell production technique, including cell parameters, is given in his thesis [2]. In Table 2.2 we summarize the parameter values relevant to our experiments. The ^{129}Xe

Cell		Rb-He	Rb-Xe
Top Cylinder	Diameter [cm]	3.66	3.8
	Length [cm]	8.0	8.2
	Wall thickness [cm]	0.095	0.1
	Volume [cm^3]	70.4	81.4
Bottom Cylinder	Diameter [cm]	2.14	2.2
	Length [cm]	29.5	11.6
	Wall thickness [cm]	0.075	0.1
	Volume [cm^3]	89.2	35.8
Transfer Tube	Diameter [cm]	1.24	1.1
	Length [cm]	5.8	6.3
	Wall thickness [cm]	0.14	0.1
	Volume [cm^3]	4.2	3.9

Table 2.2: Dimensions of ^{3}He cell (taken from [2]) and ^{129}Xe cell.

cell (see Figure 2.4), on the other hand, was filled by Ray Fuzesy who was in charge of cell production for our experiments from 2000-2001. The cell was made from quartz glass tubing in a glass shop in Berkeley, California.[4] Table 2.2 gives the cell dimensions.

[4]Unlike ^{3}He cells, ^{129}Xe cells do not require specialized glass, because of lower ^{129}Xe permeability of

Figure 2.4: ^{129}Xe cell used for NMR and EPR polarimetry studies.

The Caltech vacuum system was capable of handling low pressures (down to 10^{-8} atm) as well as high pressures (up to 6 atm). This wide range in pressure was achieved with two pumps, a turbo-molecular pump and an ion-pump, as well as valves which were able to withstand high pressures. In addition, a residual gas analyzer enabled the monitoring of the impurities in the gas system. Finally, the vacuum system had two delivery lines, one for the noble gas and one for nitrogen gas.

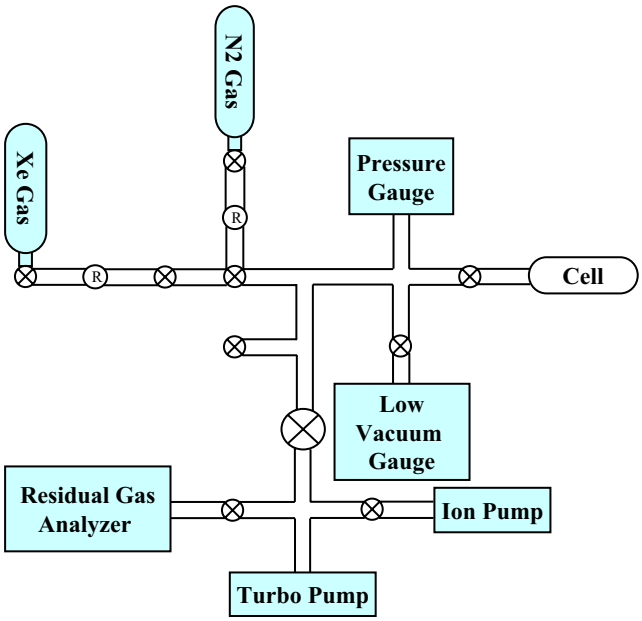

Figure 2.5: A schematics of the vacuum system used for Xe-cell production.

^{129}Xe through the glass.

2.2.3.2 Optical Pumping Setup

Optical pumping of ^{3}He and ^{129}Xe was performed with four Titanium-Sapphire (Ti-Sapph) lasers (*Spectra Physics*, model 3900S). Each Ti-Sapph laser was pumped by an Argon laser (*Spectra Physics*, model 2040E) and produced up to 5 W of tunable-wavelength laser light. The Ti-Sapph lasers have on the order of 100 times narrower bandwidth than the most commonly used diode laser, which is advantageous when pumping gas at low pressures with narrow-bandwidth absorption profiles. Figure 2.6 shows the Ti-Sapph lasers (front) and Argon lasers (back).

Figure 2.6: A photograph of the Ti-Sapphire lasers which were used for optical pumping at Caltech.

The Ti-Sapph laser beam was directed through a set of diverging lenses which expanded the beam to the size of the cell's cross section (see Figure 2.7) and then to a set of mirrors which directed the beam onto the cell. Since the laser light produced by the Ti-Sapph lasers was linearly polarized (in the horizontal direction) while optical pumping of Rb requires circularly polarized light, a quarter waveplate was placed between each laser and the cell. After passing through the quarter waveplate, the laser light was $\approx 90\%$ circularly polarized.

The cell containing the hyperpolarized gas was placed in the middle of a constant magnetic field. The field was produced by a set of Helmholtz coils which were controlled by a bipolar operational power supply (*Kepco*, model BOP 36-12M). The pumping chamber of the cell was enclosed in a homemade high-temperature resistant oven. The oven had optical windows on the front and the back for the passage of laser light and on the sides for the monitoring of the laser light absorption/fluorescence with a CCD camera.

A constant flow of hot air through the oven enabled us to heat the cells to the desired

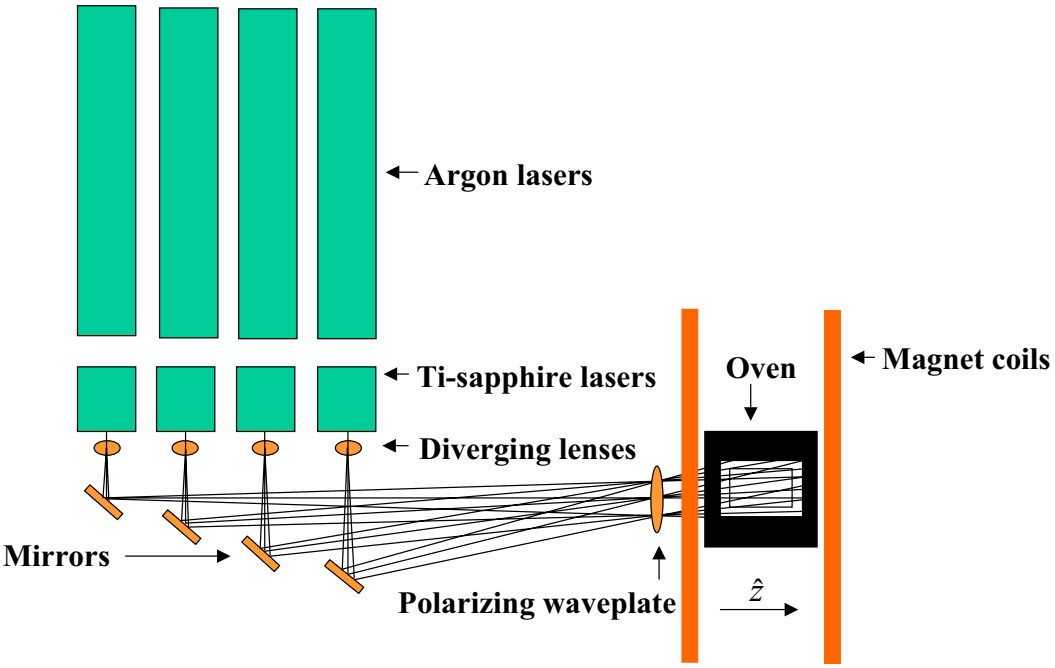

Figure 2.7: A schematics of the optical pumping setup.

temperature, which for ^{129}Xe cells was 80°-100°C, while for ^{3}He cells was 120°-150°C. The temperature was detected with a non-magnetic RTD (resistive temperature device) and monitored with a standard multimeter.

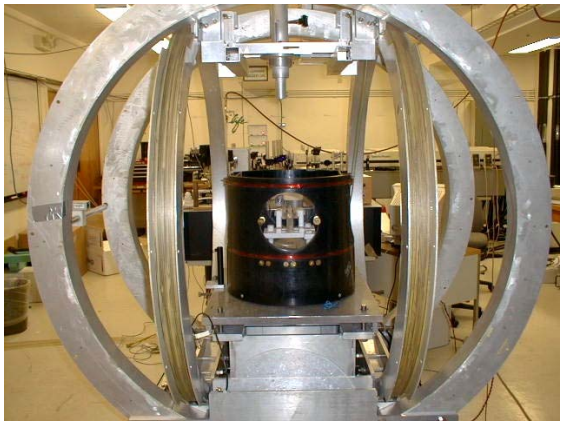

Figure 2.8: A photograph of the Helmholtz electromagnet at Caltech.

2.3 Hyperpolarized Gas NMR Polarimetry

2.3.1 NMR Polarimetry Principles

Nuclear magnetic resonance (NMR) is observed in systems that possess magnetic moment $\boldsymbol{\mu}$and spin angular momentum $\mathbf{I}$ which are related by

$$\boldsymbol{\mu} = \gamma\hbar\mathbf{I}, \tag{2.8}$$

where the constant of proportionality between the two is the gyromagnetic ratio γ. When the magnetic moments are placed in a static magnetic field, they align parallel or anti-parallel to the field to occupy the lowest energy state. The energy of a 1/2 spin particle in a field $\mathbf{B} = B_z\hat{\mathbf{z}}$ is equal to

$$E = -\gamma\hbar B_z m_z, \tag{2.9}$$

where $m_z = \pm 1/2$.

The tendency of the magnetic moments to align with the field is counter-balanced by the thermal motion which randomizes the alignment of the spins. The extent of thermal motion depends on the temperature of the sample and follows the laws of statistical mechanics. The ratio of the magnetic moments in the high energy state, $N_\downarrow$, and the magnetic moments in the low energy state, $N_\uparrow$, is proportional to the Boltzmann factor

$$\frac{N_\downarrow}{N_\uparrow} = \exp\left(-\frac{\Delta E}{kT}\right). \tag{2.10}$$

The population difference between two energy states produces a polarization of the sample. For a proton spin in a 1.5 T magnetic field and at room temperature (300 K) this thermal polarization is very small, on the order of 10^{-6}. The net macroscopic magnetization of the sample $\mathbf{M}$ is then proportional to the polarization P, the number density of the sample n, and the nuclear magnetic moment $\boldsymbol{\mu}$:

$$\mathbf{M} = \langle\boldsymbol{\mu}\rangle = \boldsymbol{\mu}\, n\, P. \tag{2.11}$$

The principle behind NMR lies in perturbing the macroscopic magnetization from its equilibrium along the z-axis by adding energy to the system in the form of radio frequency

(RF) electro-magnetic radiation, and observing the subsequent relaxation of magnetization towards its equilibrium. The RF field oscillates with rotational frequency ω and can be expressed as

$$\begin{aligned}
\mathbf{B}_1 &= 2\,B_1\,\cos(\omega t)\,\hat{\mathbf{x}} \\
&= B_1\,[\cos(\omega t)\,\hat{\mathbf{x}} + \sin(\omega t)\,\hat{\mathbf{y}}] + B_1\,[\cos(\omega t)\,\hat{\mathbf{x}} - \sin(\omega t)\,\hat{\mathbf{y}}] \\
&= B_1\,\hat{\mathbf{x}}_{rot} + B_1\,\hat{\mathbf{y}}_{rot}, \\
\hat{\mathbf{x}}_{rot} &= [\cos(\omega t)\,\hat{\mathbf{x}} + \sin(\omega t)\,\hat{\mathbf{y}}] \\
\hat{\mathbf{y}}_{rot} &= [\cos(\omega t)\,\hat{\mathbf{x}} - \sin(\omega t)\,\hat{\mathbf{y}}]\,. \qquad (2.12)
\end{aligned}$$

The second and third line of the above equation show that the RF field can be decomposed into two counter rotating components, each of magnitude B_1.

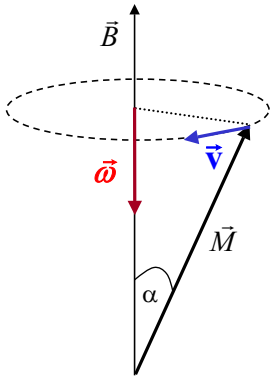

Figure 2.9: Magnetization precessing like a spinning top around the effective magnetic field $\mathbf{B}$ with a characteristic frequency ω.

The RF field flips (or tips) the magnetization away from the static field axis. When the magnetization is not parallel to the static magnetic field, it experiences a torque which causes it to precess around the net (total) field like a spinning top, with a characteristic Larmor frequency $\boldsymbol{\omega}= \gamma\mathbf{B}$ (see Figure 2.9). The equation of motion of the precessing magnetization (ignoring the relaxation processes) is equivalent to that of a spinning top:

$$\frac{d\mathbf{M}}{dt} = \mathbf{M} \times \gamma\mathbf{B}_{eff}. \qquad (2.13)$$

$\mathbf{B}_{eff}$ is the effective magnetic field, commonly expressed in a frame of reference which

is rotating with angular frequency ω around the static field and is defined by rotating coordinates $\hat{\mathbf{x}}_{rot}$ and $\hat{\mathbf{y}}_{rot}$. In this frame, only the component of B_1 field which is co-rotating with the reference frame can affect the magnetization. If the holding field along the z-axis is $B_z\hat{\mathbf{z}}$, then the effective field is

$$\mathbf{B}_{eff} = \left(B_z - \frac{\omega}{\gamma}\right)\hat{\mathbf{z}} + B_1\hat{\mathbf{x}}_{rot}. \tag{2.14}$$

If $B_z = \omega/\gamma$, the effective field has no $\hat{\mathbf{z}}$ component in the rotating frame and the magnetization aligns entirely with the $\mathbf{B_1}$ field. This is the resonance condition. In the laboratory frame, $\mathbf{B_1}$ and $\mathbf{M}$ rotate around the static magnetic field in the xy plane. The magnetic flux created by the precessing magnetization can be detected by a set of NMR receiver coils whose axes are perpendicular to $\hat{\mathbf{z}}$.

In addition to the precession around the effective magnetic field, the magnetization is subjected to the relaxation processes. There are two main types of relaxation: the T_1 relaxation is the relaxation of the longitudinal magnetization component back to thermal equilibrium levels, $M_\circ$, along the z-axis; the T_2 relaxation describes the decay of the transverse magnetization component to zero (Chapter 4 gives a detailed description of T_2 relaxation). When the relaxation processes are included into Eq. 2.13, one obtains the Bloch equations [59]:

$$\frac{d\mathbf{M}}{dt} = \mathbf{M} \times \gamma\mathbf{B}_{eff} - \frac{M_x\hat{\mathbf{i}} + M_y\hat{\mathbf{j}}}{T_2} - \frac{(M_z + M_\circ)\hat{\mathbf{k}}}{T_1}. \tag{2.15}$$

2.3.1.1 Adiabatic Fast Passage

One way to measure the polarization of hyperpolarized gas is to use the NMR technique of Adiabatic Fast Passage (AFP) [48]. In AFP, the magnetization is flipped adiabatically by 180° around x (or y) axis. The magnetization flip is achieved by either sweeping the static magnetic field B_z or the frequency ω through resonance, so that $B_z = \omega/\gamma$.

If the static magnetic field is varied in time, then B_z in Eq. 2.14 is a time-varying field $B_z(t)$. Initially, the static magnetic field is much bigger than ω/γ so that the effective field is essentially aligned with the z-axis. The static field is then varied linearly (and adiabatically) through resonance until $|B_z(t)| \gg \omega/\gamma$. Figure 2.10 schematically shows the magnetization flip.

For minimal losses of polarization to occur during the AFP sweep, two conditions must

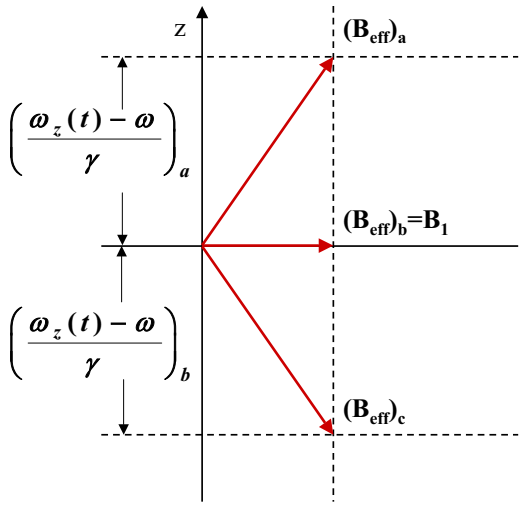

Figure 2.10: Schematics of spin-flip using the technique of the adiabatic fast passage.

be satisfied. First, the sweep must be slow enough for the magnetization to follow the effective magnetic field adiabatically. This is possible only if the rotation of magnetization around the static magnetic field in the laboratory frame (which is characterized by frequency ω) is much faster than the rotation of the effective field B_{eff}. This condition ensures that the initial relationship of magnetization with respect to the effective field remains valid throughout the sweep. Since the maximum field variation occurs on resonance, when $B_z(t) = \omega/\gamma$,

$$\left(\frac{dB_{eff}/dt}{B_{eff}}\right)_{B_z(t)=\omega/\gamma} = \frac{dB_z/dt}{B_{eff}} = \frac{dB_z/dt}{B_1}.$$

The *adiabatic* condition can then be written as

$$\frac{dB_z/dt}{B_1} \ll \omega. \tag{2.16}$$

In our NMR-AFP experiments, $dB_z/dt = 2.3$ G/s (see also Table 2.3), $B_1 \approx 0.1$ G [53], and the resonant frequency is $\omega_{He} = 2\pi f_{He} = 5.78 \times 10^5$ Hz for ^{3}He and $\omega_{Xe} = 2\pi f_{Xe} = 2.07 \times 10^5$ Hz for ^{129}Xe. Therefore, $\frac{dB_z/dt}{B_1} = 23\,\mathrm{s}^{-1} \ll \omega$.

Second, the sweep must be fast enough so that minimal transverse relaxation occurs during the sweep. This condition ensures that the magnetization vector remains constant

in length during the sweep. The *fast* condition can be written as [53]

$$\frac{D\,|\nabla B_z|^2}{B_1^2} \ll \frac{dB_\circ/dt}{B_1}, \tag{2.17}$$

where D is the gas diffusion coefficient and $|\nabla B_z|$ is the gradient of the z-component of the magnetic field.[5] Since ^{129}Xe diffusion coefficient is smaller than ^{3}He diffusion coefficient (Appendix A) due to smaller ^{129}Xe mass, it suffices to prove the fast condition for ^{3}He. The field gradients have not been measured in our experiments. However, the data presented in [53] which used our experimental setup, indicates that $|\nabla B_z|$ should at or below G/m levels. If $|\nabla B_z| \approx 1$ G/m, $B_1 \approx 0.1$ G, $D \approx 1.7 \cdot 10^{-4}$ m^2/s, then $\frac{D|\nabla B_z|^2}{B_1^2} \approx 0.017\,\mathrm{s}^{-1} \ll \frac{dB_z/dt}{B_1} = 23\,\mathrm{s}^{-1}$. Consequently, both the *adiabatic* and *fast* conditions are satisfied, so the AFP losses should be minimal (below 0.1% per sweep [53]).

It remains to determine the size of the AFP signal. The AFP signal detected in the NMR receiver coils will be proportional to the transverse magnetization component

$$M_T = M \sin\alpha = M\,\frac{(B_{eff})_T}{B_{eff}} = M\,\frac{B_1}{\sqrt{\left[B_z(t) - \frac{\omega}{\gamma}\right]^2 + B_1^2}}. \tag{2.18}$$

Equation 2.18 tells us that the AFP signal will have a Lorentzian-like shape.[6]

In addition to being proportional to the transverse magnetization, the signal size also depends on the amount of magnetic flux Φ passing through the receiver coils, the gain G^{amp} of the pre-amplifier (see section 2.3.2), and the gain G^Q associated with the Q-curve of the NMR receiver coils. All other system-dependent factors are calibrated from a source of known thermal polarization (e.g., water) and included in the factor β. The hyperpolarized noble gas and water AFP signals are, respectively,

$$\begin{aligned} S_{NG} &= \beta\, M_T^{NG}\, G_{NG}^{amp}\, \Phi_{NG}\, G_{NG}^{Q} \\ &= \beta \left\{ \mu_{NG}\, n_{NG}\, P_{NG}\, \frac{B_1}{\sqrt{\left[B_z(t) - \frac{\omega}{\gamma}\right]^2 + B_1^2}} \right\} G_{NG}^{amp}\, \Phi_{NG}\, G_{NG}^{Q} \\ &= \alpha\, \mu_{NG}\, n_{NG}\, P_{NG}\, G_{NG}^{amp}\, \Phi_{NG}\, G_{NG}^{Q} \end{aligned} \tag{2.19}$$

[5] The z-component of the total field includes the static field along $\hat{\mathbf{z}}$, as well as any gradients applied in the $\hat{\mathbf{z}}$ direction.

[6] Unlike the Lorentzian, the signal in Eq. 2.18 has a square root in the denominator.

$$S_{H_2O} \quad = \quad \alpha\, \mu_p\, n_{H_2O}\, P_{H_2O}\, G^{amp}_{H_2O}\, \Phi_{H_2O}\, G^{Q}_{H_2O}, \tag{2.20}$$

where $\alpha = \beta\, B_1 / \sqrt{\left[B_z(t) - \frac{\omega}{\gamma}\right]^2 + B_1^2}$. The thermal polarization of water (see Chapter 4.5.1 for a more detailed derivation) is

$$P \sim \frac{\hbar \gamma B_z}{2kT} = \frac{\mu_p B_z}{kT}. \tag{2.21}$$

If Eq. 2.21 is inserted into Eq. 2.20 and the constant α from Eq. 2.20 into Eq. 2.19, the hyperpolarized gas polarization is

$$P_{NG} = \frac{\mu_p}{kT} \frac{\frac{\omega}{\gamma}}{} \frac{S_{NG}}{S_{H_2O}} \frac{\mu_p}{\mu_{NG}} \frac{n_{H_2O}}{n_{NG}} \frac{G^{amp}_{H_2O}}{G^{amp}_{NG}} \frac{\Phi_{H_2O}}{\Phi_{NG}} \frac{G^{Q}_{H_2O}}{G^{Q}_{NG}}. \tag{2.22}$$

2.3.2 NMR Electronics

NMR Parameters	Water	He	Xe
Field Sweep (Gauss)	18.0-28.3	18.9-29.2	21.3-31.6
Sweep Rate (G/s)	2.34	2.34	2.34
Pre-Amp Gain	100	10	100
RF Amp Gain (Volts)	50	50	50
Q-Curve Gain (relative)	1	1	0.09
f_{RF} (kHz)	92	92	33
B_{res} (Gauss)	21.6	28.4	27.8

Table 2.3: Parameter values during the NMR-AFP experiment.

Figure 2.11 shows the schematics of the NMR electronics. A static magnetic field which is produced by a set of Helmholtz coils defines the z-axis. The other two sets of axes are defined by the RF coils and the NMR receiver coils.

The AFP signal from both receiver coils was added up and amplified in a pre-amplifier (*Stanford Research Systems*, model SR560). Because the receiver coils were not perfectly perpendicular to the RF coils, they picked up not only the AFP signal, but also some residual driving RF field, which was produced by amplifying the output of a function generator (amplifier: *EIN*, model 2100L). However, unlike the AFP signal, the RF pick-up signal was nearly 180° phase-shifted in the two NMR coils. By adding the signals from the two coils, the RF pick-up should have cancelled completely. In reality, the cancellation was not

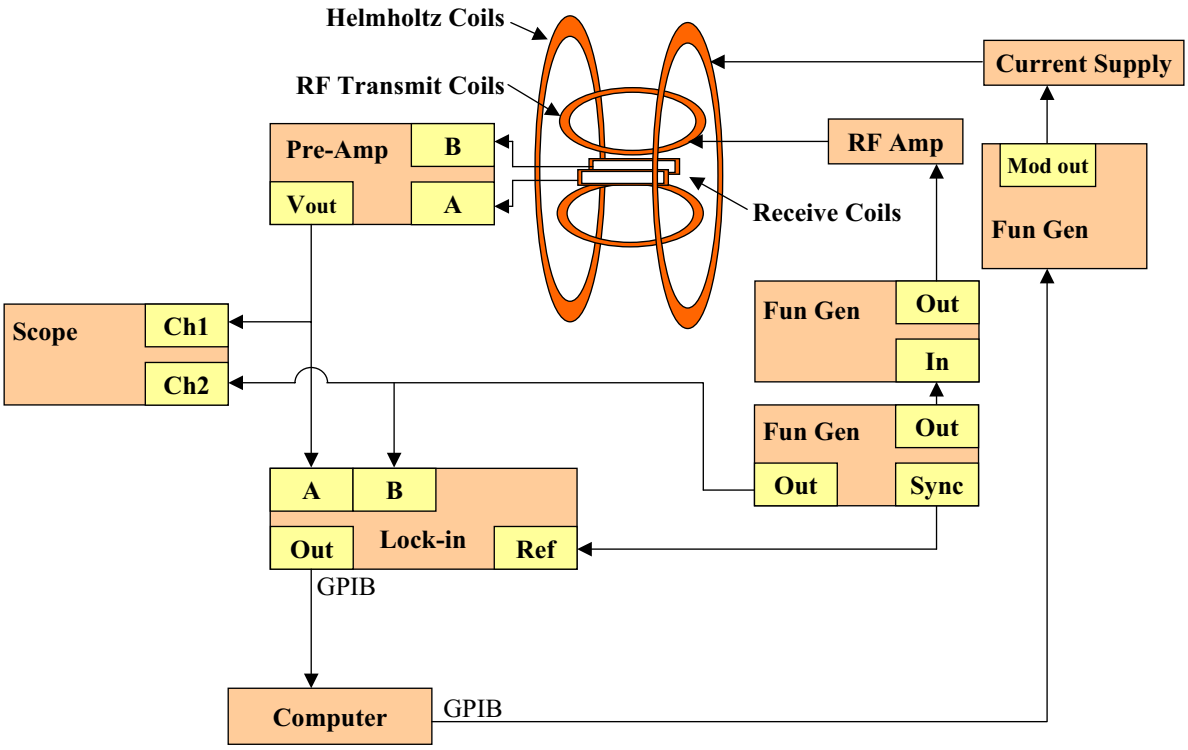

Figure 2.11: Electronic circuitry for NMR detection.

perfect, and there was still a small residual RF signal in the output of the pre-amplifier. A lock-in amplifier (*Stanford Research Systems*, model SR830 DSP), an oscilloscope and a function generator (*Hewlett Packard*, model 33120A) with an adjustable amplitude and phase and with frequency locked to the radio-frequency, were used to cancel the residual RF pick-up field. Values of the main NMR parameters are listed in Table 2.3.

A LabView program and a function generator (*Hewlett Packard*, model 3325B) controlled the field sweep.[7] The holding field was swept ± 10.3 G (usually starting at around 18 G) in 8.8 s (at a rate of 2.34 G/s), which resulted in two spin flips and, therefore, two AFP signals (see Figure 2.12). The resulting signal was recorded by the computer and displayed in *LabView*.

[7]Note that in the NMR experiment, the AFP sweep can only be performed by sweeping the B_z field through resonance. Sweeping the frequency through resonance is not feasible because the cancellation of the residual RF pick-up can only be performed at a single (constant) frequency.

2.3.3 Water NMR Signals and Water Thermal Polarization

From Eq. 2.20, the water signal is

$$\begin{aligned} S_{H_2O} &= \beta \frac{B_1}{\sqrt{\left[B_z(t) - \frac{\omega}{\gamma}\right]^2 + B_1^2}} \mu_p \, n_{H_2O} \, P_{H_2O} \, G^{amp}_{H_2O} \, \Phi_{H_2O} \, G^{Q}_{H_2O} \\ &= \beta \frac{M \, G^{amp}_{H_2O} \, \Phi_{H_2O} \, G^{Q}_{H_2O}}{\sqrt{\left[\frac{B_z(t) - \frac{\omega}{\gamma}}{B_1}\right]^2 + 1}}. \end{aligned} \tag{2.23}$$

Therefore, if we fit the AFP signals with a function of the form

$$\frac{A}{\sqrt{\left[\frac{x - x_\circ}{\Delta x}\right]^2 + 1}} + a\,x^2 + b\,x + c,$$

then $A = \beta \; M_{H_2O} \; G^{amp}_{H_2O} \; \Phi_{H_2O} \; G^{Q}_{H_2O}$, $x = B_z(t)$, $x_\circ = B_{res} = \omega/\gamma$, $\Delta x = B_1$. The quadratic function in x was added to account for the changing background during the AFP flip. Computing water thermal polarization using Eq. 2.21 at the resonant field values we can then find the calibration constant β. In addition, the width of the resonance gives a measure of the B_1 strength. Table 2.4 gives values of the parameters used in the calibration of β for ^{3}He and ^{129}Xe and the corresponding uncertainties.

Water Parameter	^{3}He NMR-AFP calibration		^{129}Xe NMR-AFP calibration	
	Value	Uncertainty	Value	Uncertainty
μ_p (eV/G)	$8.803\times10^{-12} = 2.7928\mu_N$	-	$8.803\times10^{-12} = 2.7928\mu_N$	-
γ (Hz/G)	4258	-	4258	-
kT@25°C (eV)	0.0257	2%	0.0257	2%
f_{RF} (kHz)	92	0.5%	92	0.5%
n_{H2O}@25°C (amg)	2489.4	0.5%	2489.4	0.5%
A_{H2O} (from fit)	3.85×10^{-5}	2.5%	4.8×10^{-5}	2.5%
G^{amp}_{H2O}	100	0.5%	100	0.5%
G^{Q}_{H2O} (r.u)	1	-	1	-
$\Phi_{H2O} \propto r^2_{H2O}$ (cm)	$(0.9)^2$	2.5%	1	2.5%

Table 2.4: Parameters related to water AFP signal.

Note that the above analysis ignores T_1 and T_2 water relaxation during the AFP flip. To account for the relaxation processes the AFP resonances should be modelled using the Bloch equation (Eq. 2.15), as was done in [53, 54]. The results in these works show that the two APF resonances (the resonance during the up-ramp and the resonance during the down-ramp of the magnetic field) have slightly different amplitudes. However, to first order, it suffices to approximate the amplitude of the water thermal signal with the average amplitude of the two AFP resonances and the thermal water polarization with the average thermal polarization at the two resonant field values [2].

Figure 2.12 shows water AFP signals and the corresponding fits that were used in the calibration of ^{3}He and ^{129}Xe polarization.

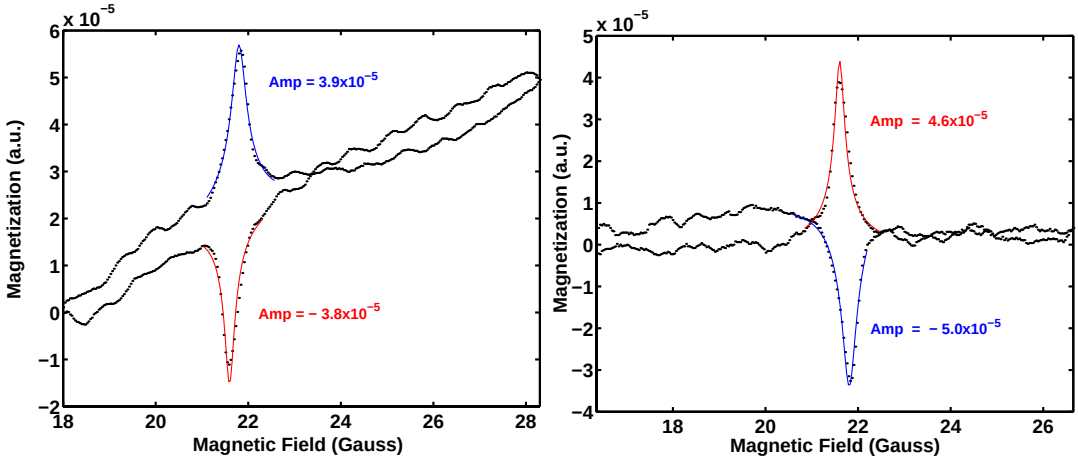

Figure 2.12: Water AFP signals used for calibration of ^{3}He polarization (left) and ^{129}Xe polarization. Left: $A_1 = 3.9 \times 10^{-5}$, $B_{res} = 21.8$ G, $\Delta B_1 = 0.15$ G; $A_2 = -3.8 \times 10^{-5}$, $B_{res} = 21.6$ G, $\Delta B_2 = 0.10$ G. Right: $A_1 = 4.6 \times 10^{-5}$, $B_{res} = 21.6$ G, $\Delta B_1 = 0.1$ G; $A_2 = -5.0 \times 10^{-5}$, $B_{res} = 21.8$ G, $\Delta B_2 = 0.15$ G.

2.3.4 ^{3}He and ^{129}Xe NMR Polarimetry

Before we can compute ^{3}He and ^{129}Xe polarizations, Eq. 2.22 has to be adjusted slightly. To account for the fact that the top cylinder is heated, while the bottom one is not, we need to replace the gas number density n_{NG} with the number density in the bottom cylinder n_b where the NMR signal is measured. We can do so by multiplying n_{HG} with

$$\frac{n_b}{n_{HG}} = \frac{V}{V_b + (V - V_b)\frac{T_b}{T_t}}, \tag{2.24}$$

where V is the total volume of the cell, V_b is the volume of the bottom cylinder, T_b is the temperature in the bottom cylinder ($\approx 50°$C for ^{3}He and $\approx 40°$C for ^{129}Xe), while T_t is the temperature in the top cylinder (150°C for ^{3}He and 100°C for ^{129}Xe). Similarly, the noble gas number density in the top cylinder can be adjusted by computing the factor n_t/n_{HG}, where

$$\frac{n_t}{n_{HG}} = \frac{V}{V + V_b\left(\frac{T_t}{T_b} - 1\right)}. \tag{2.25}$$

Finally, the ratio of the water and noble gas magnetic fluxes through the NMR pick-up coils is proportional to the ratio of the diameters of the bottom cylinders [2]:

$$\frac{\Phi_{H_2O}}{\Phi_{NG}} \propto \frac{r^2_{H_2O}}{r^2_{NG}}. \tag{2.26}$$

^{3}He and ^{129}Xe polarizations can now be computed from Eq. 2.22 using water parameters from Table 2.4 and ^{3}He and ^{129}Xe parameters from Tables 2.5 and 2.6, respectively. For the ^{3}He data displayed in Figure 2.13 we obtain

$$P^{NMR}_{He} = 10.4\%.$$

Similarly, for the ^{129}Xe data displayed in Figure 2.14 the ^{129}Xe polarization is

$$P^{NMR}_{Xe} = 6.5\%.$$

The uncertainties in the parameters are given in Tables 2.4, 2.5 and 2.6. The main sources of systematic uncertainty for water are: the temperature at which the thermal polarization is being evaluated (room temperature of 25°C is assumed), the thickness of the cell's glass and thus the radius of the bottom cylinder, and the amplitude of the signal from the fit. For ^{3}He and ^{129}Xe the main source of systematic uncertainty comes from the fit. An additional error when calibrating the ^{129}Xe signal is due to the adjustment in the Q-curve gain. When all the systematic uncertainties are added in quadrature, we obtain $\approx 7\%$ uncertainty in the ^{3}He and ^{129}Xe NMR polarization measurement.

Helium Parameter		
	Value	Uncertainty
μ_{He}	$-2.12762\mu_N$	-
γ (Hz/G)	3243	-
T_{pump} (^oC)	150	1.2%
f_{RF} (kHz)	92	0.5%
n_{He} (amg)	7.66	1%
n_b/n_{He}	1.11	2.5%
A_{He} (from fit)	0.1675	4%
G^{amp}_{He}	10	0.5%
G^{Q}_{He}	1	-
$\Phi_{He} \propto r^2_{He}$	$(0.99)^2$	2%

Table 2.5: Parameters related to helium AFP signal.

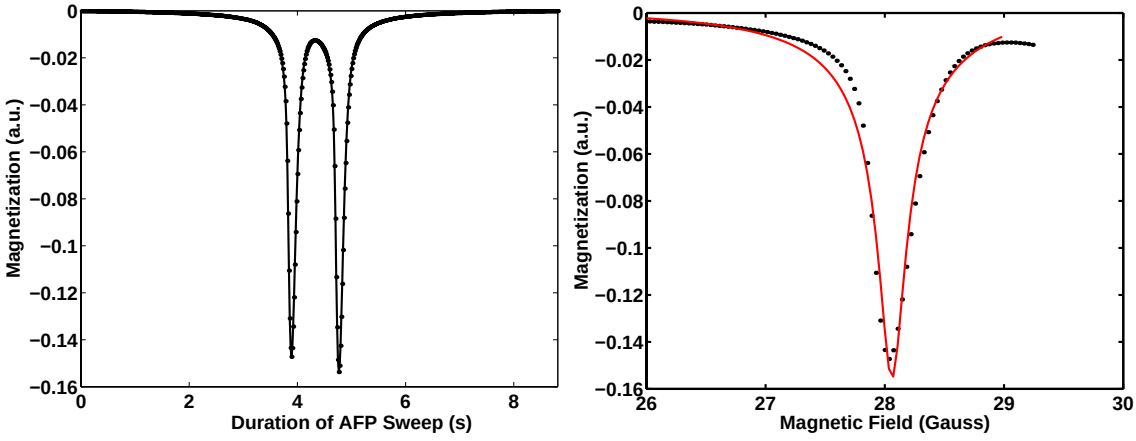

Figure 2.13: Left: ^{3}He AFP signal as a function of time. Right: AFP resonance during the ramp-up time and best fit to the data, $A_1 = -0.1639$, $B_{res} = 28.6$ G, $\Delta B_1 = 0.11$ G.

Xenon Parameter		
	Value	Uncertainty
μ_{Xe}	$-0.7768\mu_N$	-
γ (Hz/G)	1186	-
T_{pump} (^oC)	100	1.3%
f_{RF} (kHz)	33	0.5%
n_{Xe} (amg)	0.024	1%
n_b/n_{Xe}	1.12	2.5%
A_{Xe} (from fit)	1.12×10^{-4}	4%
G^{amp}_{Xe}	100	0.5%
G^{Q}_{Xe}	0.09	2%
$\Phi_{Xe} \propto r^2_{Xe}$	$(1)^2$	2%

Table 2.6: Parameters related to xenon AFP signal.

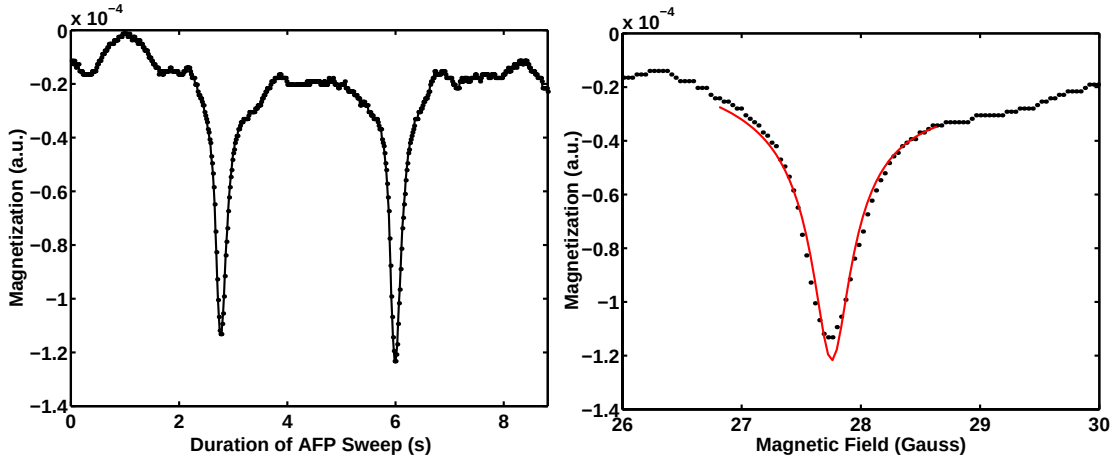

Figure 2.14: Left: ^{129}Xe AFP signal as a function of time. Right: AFP resonance during the ramp-up time and best fit to the data, $A_1 = -1.08 \times 10^{-4}$, $B_{res} = 27.8$ G, $\Delta B_1 = 0.15$ G.

2.4 Hyperpolarized Gas EPR Polarimetry

2.4.1 EPR Polarimetry Principles

Another method for determining the polarization of noble gases is based on the frequency shift of the ^{85}Rb Zeeman resonance (or electron paramagnetic resonance – EPR), which results from the buildup of noble gas polarization. This polarimetry method was first explored on hyperpolarized ^{129}Xe by Schaefer *et al.* [5] and further developed into a robust method for measuring polarization levels of ^{3}He by Newbury *et al.* [4], Barton *et al.* [60] and Romalis *et al.* [3].

The Zeeman resonance is dependent on the background field experienced by the atom. For the $F = I + 1/2$, $m = \pm F$ state, the dependence is expressed in the Breit-Rabi equation [61],

$$\frac{d\nu_{EPR}(F,m)}{dB} = \frac{\mu_B g_e}{h(2I+1)}\left(1 + \frac{8I}{(2I+1)^2}\,\frac{\mu_B g_e B}{hA}\right), \tag{2.27}$$

where μ_B is the Bohr magneton, $g_e = 2.00232$ for the electron and h is the Planck constant. For ^{85}Rb, $I = 5/2$ and $A = 1023$ MHz [3]. In the limit of low magnetic fields (below 10 G [53]), the EPR frequency is proportional to the magnetic field (the constant of proportionality is $\gamma_{Rb}/2\pi = \mu_B g_e/h[2I+1]$). At higher magnetic fields, the contribution from the quadratic term will become progressively more significant.

Apart from the static holding magnetic field, two additional factors influence the background field. First, the magnetization of the noble gas produces a dipole field, B_{dipole}, which adds to the holding field.[8] This classical magnetic field is proportional to the magnetization of the noble gas, $B = C\,M$, where C is a dimensionless constant when using the Gaussian unit system. For a spherical geometry $C = 8\pi/3$. Therefore, the EPR frequency shift due to the classical magnetic field produced by the gas magnetization M is

$$\Delta\nu_M = \frac{d\nu(F,m)}{dB}\,B_{dipole} = \frac{d\nu(F,m)}{dB}\,\frac{8\pi}{3}\,M. \tag{2.28}$$

The second contribution to the background field originates from the Fermi contact interaction which produces spin exchange between the ^{85}Rb electron and the nucleus of the

[8] Only the component of the dipole field parallel to the holding field contributes to the EPR shift to a significant degree [3].

noble gas. The EPR frequency shift due to the spin exchange is equivalent to [3]

$$\Delta\nu_{SE} = \frac{d\nu(F,m)}{dB}\, B_{SE} = \frac{d\nu(F,m)}{dB}\, \frac{2\,\hbar\, K_{SE}\, \langle v\, \sigma_{SE}\rangle\, n_{NG}}{g_e \mu_B} K_z, \tag{2.29}$$

where K_{SE} is the ratio of the imaginary and real parts of the spin-exchange cross section [3], n_{NG} is the hyperpolarized gas number density, K_z is the z-component of the nuclear spin, and $\langle v\, \sigma_{SE}\rangle$ is the velocity average of the real part of the spin-exchange cross section, σ_{SE}.

The classical (Eq. 2.28) and spin-exchange (Eq. 2.29) contributions to the EPR frequency shift are both proportional to the noble gas polarization $P = K_z/K$, and number density n_{NG}. They can therefore be combined into a single expression,

$$\Delta\nu_{EPR} = \Delta\nu_M + \Delta\nu_{SE} = \frac{8\pi}{3}\, \frac{d\nu(F,m)}{dB}\, \kappa_\circ\, \mu_{NG}\, n_{NG}\, P, \tag{2.30}$$

where μ_{NG} is the magnetic moment of the noble gas and $\kappa_\circ$ is a dimensionless constant that depends on temperature, but not on the density or the polarization of the noble gas. Note that if the EPR frequency shift was solely due to the classical field produced by the noble gas magnetization in a spherical geometry, $\kappa_\circ = 1$. Therefore, a value of $\kappa_\circ$ which is bigger than one represents an enhancement resulting from the spin exchange between the Rb electron and the noble gas nucleus.[9] Table 2.7 gives theoretical and experimental $\kappa_\circ$ values for ^{3}He and ^{129}Xe (from [3, 4, 5]).

$\kappa_\circ$ Values	Rb-He	Rb-Xe
Experimental	4.52 + 0.00934 T[°C]	644 ± 260
Theoretical	2.7-8.8	726

Table 2.7: Experimental and theoretical values of $\kappa_\circ$ for Rb-He and Rb-Xe interaction. Rb-He experimental value taken from [3]; Rb-He theoretical value taken from [4]; Rb-Xe experimental and theoretical values taken from [5].

Finally, if we substitute Eq. 2.27 into Eq. 2.30 and express the noble gas polarization in

[9] $\kappa_\circ$ is often called the *enhancement* factor.

terms of the EPR frequency shift in a spherical cell, we obtain

$$P_{NG} = \Delta\nu_{EPR} \left\{ \frac{8\pi}{3} \frac{\mu_B g_e}{h(2I+1)} \left(1 + \frac{8I}{(2I+1)^2} \frac{\mu_B g_e B}{hA} \right) \kappa_\circ \, \mu_{NG} \, n_{NG} \right\}^{-1}. \tag{2.31}$$

2.4.2 EPR Electronics

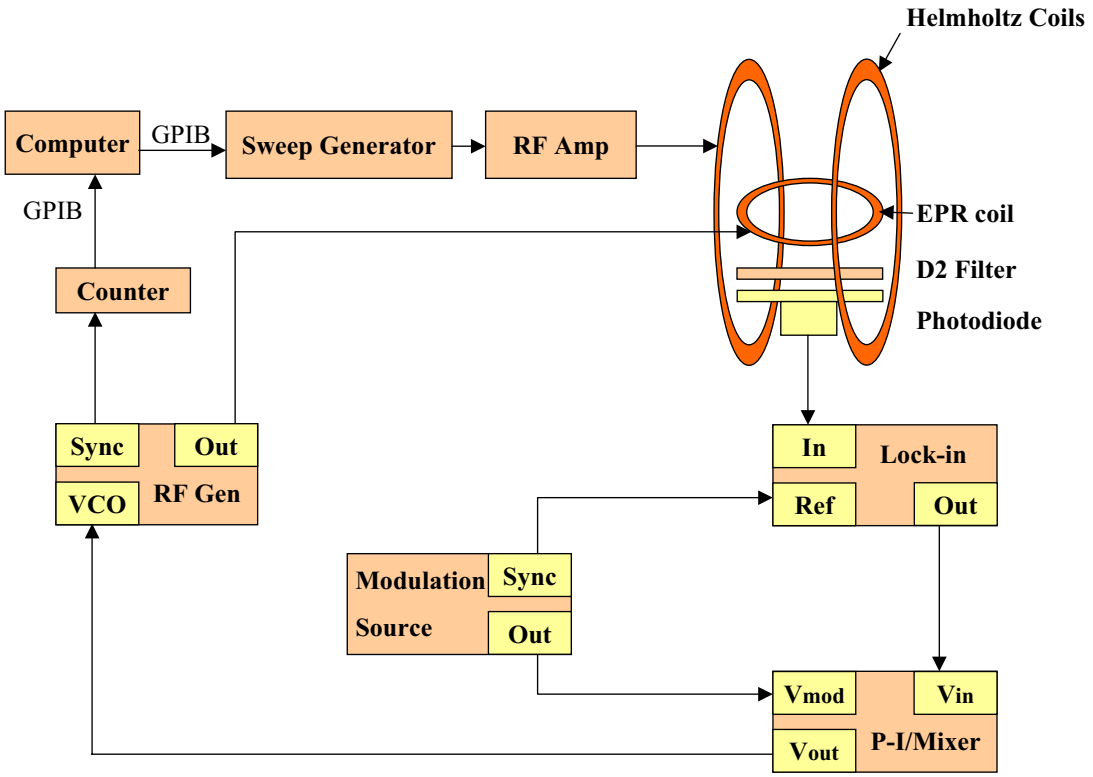

Figure 2.15: Electronic circuitry for EPR detection.

The EPR electronics setup is schematically presented in Figure 2.15. The circuitry detects Rb electron paramagnetic resonance and traces shifts in the central resonant frequency which result from the variations in the background magnetic field.

During optical pumping, most of rubidium vapor is polarized (between 60% and 90% [53]). This means that laser light can penetrate deep into the cell without being absorbed. However, if the level of rubidium polarization is suddenly reduced, the efficiency of optical pumping increases. We made use of this causal relationship during the EPR detection. Rubidium polarization was decreased using a solenoid surface coil (EPR coil) which excited the transitions of rubidium's atoms from the $(F = 3, m_F = 3)$ state to the $(F = 3, m_F = 2)$

state.[10] As the absorption of laser light increases, the decay of atoms back into the ground state increases as well. Most of the atoms are radiationlessly quenched to the ground state by the nitrogen in the cell. However, a small fraction (3-5%) of them [53] decay by emitting either a D1 or D2 fluorescence photon (see Figure 2.1). The D2 fluorescence was detected by a photodiode (*New Focus*, model 2031) and a D2 filter (*Newport*). We chose to detect D2 rather than D1 fluorescence because the laser light, which was also tuned to the D1 transition, could have saturated the photodiode. By monitoring the intensity of D2 transitions as a function of radio-frequency, we would be able to detect the electron paramagnetic resonance.

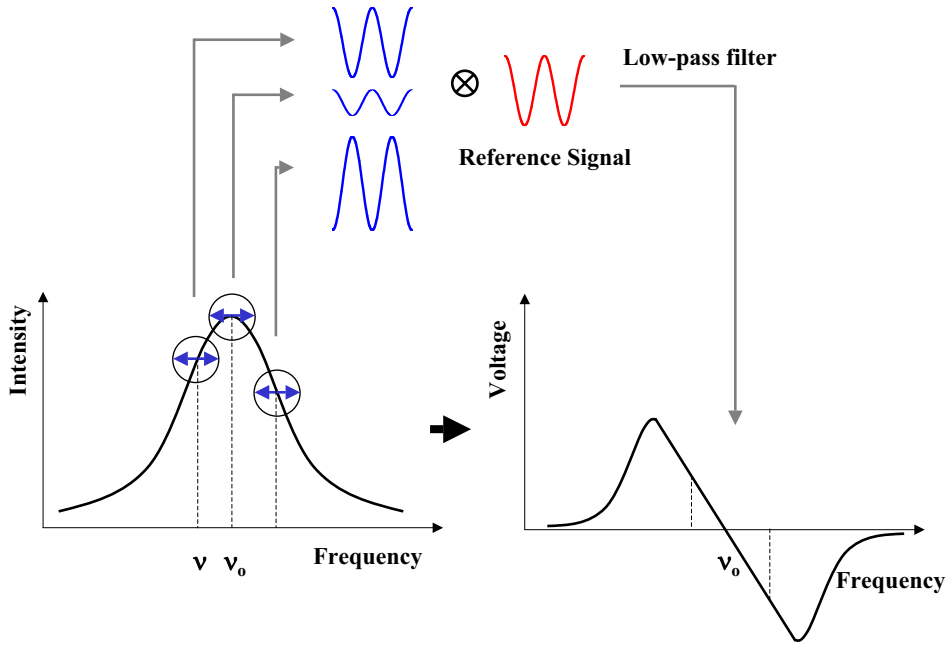

Figure 2.16: Modulation of the Zeeman resonance produces a dispersion curve.

However, instead of monitoring the intensity of D2 fluorescence, we monitored the *changes* in the D2 fluorescence while frequency-modulating the EPR excitation signal. The frequency modulated D2 signal was detected by a lock-in amplifier (*Stanford Research Systems*, model SR830 DSP) which was referenced to the modulation source (*Hewlett Packard*, model 33120A).[11] The lock-in amplifier's output was a DC signal that was proportional

[10] Because the magnetic field produced by the EPR coil is linearly polarized along the x-axis, while the Zeeman splitting is along the z-axis, the EPR coil will produce oscillatory transitions from the $m_F = 3 \rightarrow 2$ state as well as from the $m_F = -3 \rightarrow$-2 state. Consequently, the sense of the circular polarization of laser light has no effect on the EPR excitations.

[11] In ^{129}Xe EPR polarimetry experiments, an additional amplifier (*Stanford Research Systems*,

to the RMS (root-mean-square) voltage of the modulated D2 fluorescence[12]. For instance, modulating the central frequency of the EP resonance gives a zero DC signal, while modulating the frequency which is to the left of the central resonance results in a positive DC signal. Consequently, the output of the lock-in amplifier produced a derivative of the D2 resonance, which is a dispersion curve. This is depicted in Figure 2.16. To see this formally, consider a signal intensity I around a frequency point $\nu_\circ$. If the frequency is modulated with a modulation signal of amplitude $\Delta\nu$ and frequency ν_{mod}, then the signal intensity can be written as $I\left(\nu_\circ + \Delta\nu \sin\left(2\pi\nu_{mod}t\right)\right)$. In the limit of small modulation amplitudes, the signal intensity can be expended in a Taylor series:

$$I\left(\nu_\circ + \Delta\nu \sin\left(2\pi\nu_{mod}t\right)\right) \approx I(\nu_\circ) + \frac{dI}{d\nu}\Delta\nu \sin\left(2\pi\nu_{mod}t\right). \tag{2.32}$$

The $I(\nu_\circ)$ term is a DC offset which is removed when using AC coupling on the lock-in amplifier. The second term, $\frac{dI}{d\nu}\Delta\nu \sin\left(2\pi\nu_{mod}t\right)$, is a sine wave of amplitude $\frac{dI}{d\nu}\Delta\nu$ and frequency ν_{mod}. The output of the lock-in will be proportional to the RMS voltage of this signal and, therefore, to the derivative of the resonance $dI/d\nu$. Furthermore, if $\Delta\nu$ is small enough so Eq. 2.32 is a valid approximation, the lock-in output is also proportional to $\Delta\nu$, which means that a bigger EPR signal can be produced by increasing $\Delta\nu$ (see region of linearity near $\nu_\circ$ in the dispersion curve of Figure 2.16). In practice, $\Delta\nu$ was approximately one third of the resonance width (see Table 2.8 for the parameter values used in the EPR measurement).

The derivative of the D2 resonance served as a feedback signal to trace shifts in the central frequency of the EPR curve [5]. When the frequency of excitation matches the EP resonance, the derivative and thus the feedback signal are zero. When the frequency is less than the resonant frequency, the derivative is a positive signal. If this positive signal is converted into a positive frequency shift, the radio-frequency could be shifted back to the resonance.

The feedback was achieved with the proportional integrator shown in Figure 2.17. The

model SR560) was used to amplify and filter the signal from the photodiode before detecting it by a lock-in amplifier.

[12]The lock-in amplifier multiplies the input signal with the reference signal of a specific frequency and then passes this product through a low-pass filter which performs the averaging (integration) of the product. After the integration, the only nonzero component results from part of the input signal which was at the same frequency as the reference frequency.

EPR Parameters	He	Xe
Frequency Sweep (kHz)	92-30	43-3
B(Gauss)	18.9	18.9
f_{Res} (kHz)	61.3	22.4
Pre-Amp Gain	-	2
Lock-in Time Constant (s)	0.3	0.3
Modulation Freq. (Hz)	300	300
Modulation Amp. (kHz)	+/- 20	+/- 20
EPR Frequency (MHz)	8.8	8.8
RF Amp Gain (Volts)	50	50

Table 2.8: Parameter values during the EPR-AFP experiment.

output of the mixer which adds the modulation signal and the feedback was sent to a voltage controlled oscillator input of a RF function generator (*Wavetek*, model 80). The VCO converted the amplitude of the input signal into a frequency offset. The output of the RF function generator was therefore: $\nu_{RF} = \nu_\circ + \nu_{feedback} + \Delta\nu \sin(2\pi\nu_{mod}t)$, where $\nu_\circ$ was set on the function generator, $\nu_{feedback}$ was the frequency shift resulting from the lock-in output and the proportional integrator, and the last term was due to the modulation signal. A counter (*Hewlett Packard*, model 53181A) was used to read off the frequency from the RF function generator, while a LabView program recorded the values on the counter.

To isolate the shift in the EPR frequency due to the magnetization of noble gas, the gas magnetization was flipped by 180° using adiabatic fast passage method described in Chapter 2.3.1.1. However, unlike in the NMR polarimetry, we swept the frequency rather than the magnetic field because the magnetic field had to be stable during the EPR measurement. Figure 2.18 shows, schematically, the change in the EPR frequency when the noble gas magnetization is flipped by 180°. Recording the EPR frequency before and after the AFP flip enables an estimation of the EPR shift and, consequently, the noble gas polarization. Formally, $\Delta\nu_{EPR} \propto \{B_z + M_{NG} - (B_z + M_{NG})\} \propto 2M_{NG}$.

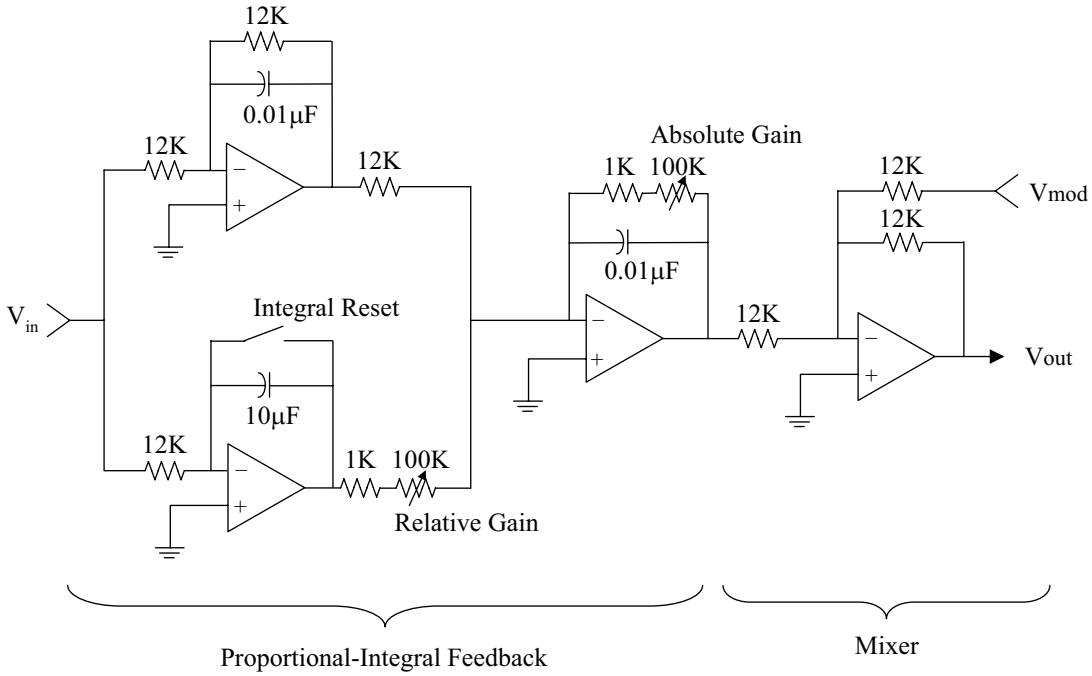

Figure 2.17: Proportional-integral feedback and mixer circuitry.

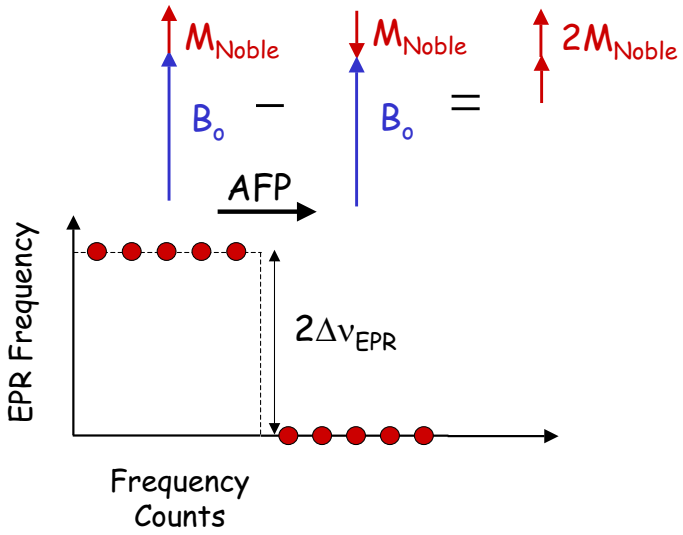

Figure 2.18: Schematics of EPR frequency before and after AFP flip.

2.4.3 ^{3}He and ^{129}Xe EPR Polarimetry

Using the parameter values listed in Table 2.9 we can simplify Eq. 2.31 so that

$$P_{NG} = 0.862 \left[\frac{amg}{kHz}\right] \frac{\Delta\nu_{EPR}}{\kappa_\circ \, n_{NG} \left(\frac{n_t}{n_{NG}}\right)}, \tag{2.33}$$

where we used the fact that $[\text{amg} \cdot \text{erg/G}] = 44.5 \times 10^{-6}\, \text{N}_\text{A}[\text{G}]$, where N_A is the Avogadro constant. Also, since the EPR signal is acquired in the top chamber, the hyperpolarized gas number density had to be adjusted by the factor n_t/n_{HG}.

ERP-related Parameters	Value
μ_B (erg/G)	9.2741×10^{-21}
γ (kHz/G)	466
h (erg s)	6.626×10^{-27}
I(^{85}Rb)	5/2
g_e	2.00232
A (MHz)	1023

Table 2.9: Parameter values related to EPR Polarimetry.

	^{3}He EPR		^{129}Xe EPR	
	Value	Uncertainty	Value	Uncertainty
n_{HG} (amg)	7.66	1%	0.02422	1%
n_t/n_{HG}	0.85	2.5%	0.72	2.5%
μ_{HG} (erg/G)	-1.0746×10^{-23}	-	-3.9230×10^{-24}	-
κ_o	4.52 + 0.00934 T[°C]	1.5% (i) 1.3% (ii)	726	(theory estimation)
$\Delta\nu_{EPR}$	4533	6%	1812	50%

Table 2.10: Helium and xenon parameters used in EPR polarimetry. $^{(i)}$Uncertainty related to $\kappa_\circ$ measurement. $^{(ii)}$Uncertainty due to the non-spherical shape of the cell.

The ^{3}He EPR signal is shown in Figure 2.19. This data was collected immediately

after collecting ^{3}He NMR-AFP data displayed in Figure 2.13. Therefore, the polarizations obtained with the EPR and NMR methods should agree within the error bars. From the data in Figure 2.19 we find that $\Delta\nu_{EPR} = 4533 \pm 270$ Hz. Using Table 2.10, ^{3}He polarization is

$$P_{He}^{EPR} = 10.2\%.$$

The main uncertainty in the ^{3}He EPR data comes from the estimation of the EPR shift. Due to background field instability, the EPR frequency shifts with time. For the data displayed in Figure 2.19 the standard deviation of frequency shift was ± 265 Hz. However, the frequency shift can be even bigger if the feedback does not function properly. In addition, since the cells used in our experiments were cylindrical rather than spherical, the enhancement factor $\kappa_\circ$ has an additional 1.3% uncertainty associated with it [3]. The total uncertainty in the estimation of ^{3}He polarization using the EPR polarimetry method was thus $\approx 7\%$.

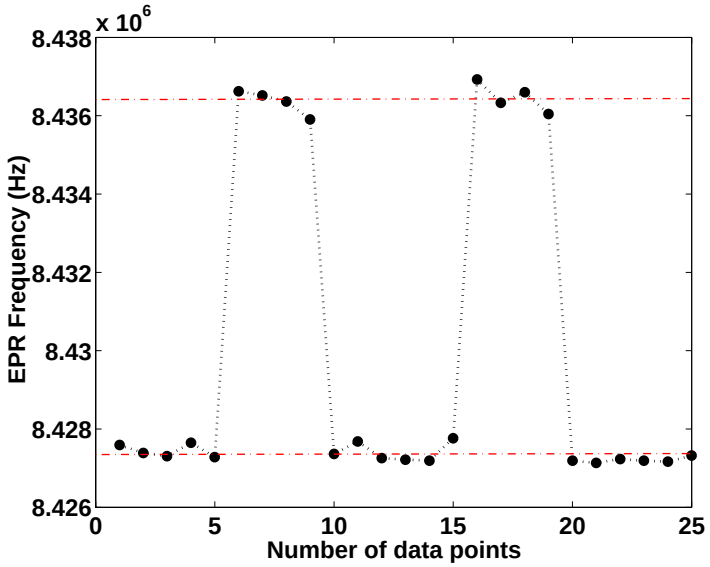

Figure 2.19: Helium EPR frequency shifts after AFP flip.

To analyze our ^{129}Xe EPR data, it is useful to compute the predicted frequency shift due to 6.5% ^{129}Xe polarization, as indicated by the NMR polarimetry data. Using the parameter values listed in Table 2.10 and relying on the theoretical value for Rb-Xe $\kappa_\circ$ constant, we obtain a frequency shift of approximately 500 Hz. Although the total frequency shift after an AFP flip should be around 1 kHz, our measurements gave a shift on the order of 3.5 kHz

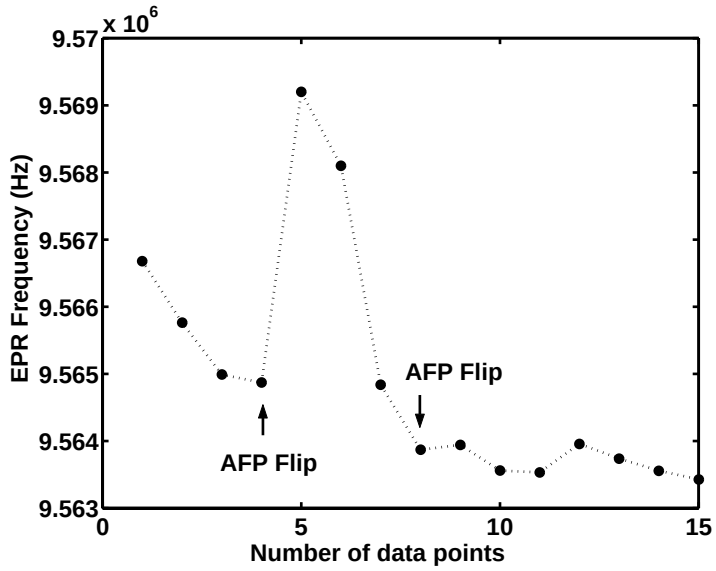

Figure 2.20: A preliminary xenon EPR frequency shift after one AFP flip.

(Figure 2.20). However, the uncertainty in this measurement is large due to the following possible reasons:

1. The background EPR frequency in Figure 2.20 is shifting significantly, either due to the magnetic field instability or due to poor feedback control. The magnetic field instability could be reduced, in the future, by using a magnetic flux magnetometer to monitor the magnetic field and correct for the field jitter (or drift) by employing a feedback loop similar to the one used in the EPR polarimetry. Romalis *et al.* [3] used a flux-gate magnetometer for ^{3}He EPR polarimetry measurements. The feedback control, on the other hand, was challenging due to the small Rb resonance signals generated in the ^{129}Xe cell in contrast to the ^{3}He cell. Because optical pumping of ^{129}Xe cell is performed at 80°C when Rb-^{129}Xe spin-exchange is most effective, while optical pumping of ^{3}He requires temperatures of around 150°C, the rubidium number density in the ^{129}Xe cell is two orders of magnitude smaller than in the ^{3}He cell. Since the intensity (amplitude) of the detected D2 light is proportional to the number of Rb transitions, this reduction in temperature leads to a small Rb resonant signal. In the future, we could try to polarize ^{129}Xe at 80°C, and then increase the temperature to 150°C to detect the Rb resonance. However, since the spin-destruction rate due to Xe-Rb collisions would increase at higher temperature, the relaxation time of hyperpolarized gas would decrease as well.

2. Figure 2.20 also indicates that after the initial AFP flip the ^{129}Xe polarization was lost, as there is no observable shift after the second AFP flip. Furthermore, judging from the decay of the EPR frequency immediately after the initial shift, it appears that the ^{129}Xe magnetization decayed while being anti-aligned with the magnetic field. This could occur, for instance, if the AFP flip was incomplete. If the gas magnetization was partly left in the transverse plane, the gas would be subject to T_2^* decay (i.e., decay due to the field inhomogeneities; see Chapter 4 for further details.). More importantly, if the lifetime (i.e., $1/\Gamma$) of the cell was very short (on the order of one minute), then the gas magnetization would have decayed to zero in time $t = \ln 2/(\gamma_{SE} + \Gamma) \approx 40$ s, where the spin-exchange rate γ_{SE} is on the order of 10^{-4} s^{-1} for ^{129}Xe at 90°C. Since each point in Figure 2.20 was an average over 5 s, the gas magnetization was anti-aligned with the magnetic field for 20 s. For a cell with poor lifetime, this could have been long enough for polarization to decay to zero.

3. An additional obstacle in implementing EPR polarimetry on ^{129}Xe is the fact that ^{129}Xe is best polarized at low gas pressures [45]. Low number density results in low gas magnetization levels and, therefore, in an inherently small average EPR frequency shift. EPR polarimetry is for now best suited for high-pressure ^{3}He targets used in nucleon spin structure function experiments which produce large frequency shifts (10 kHz and more).

2.5 Concluding Remarks

We have successfully implemented the EPR polarimetry for measuring polarizations of hyperpolarized ^{3}He. By measuring the EPR frequency shift in rubidium, we estimated $10.2\% \pm 0.7\%$ of ^{3}He polarization. This result was supported by NMR polarimetry data, which gave a ^{3}He polarization of $10.4\% \pm 0.7\%$. The ^{129}Xe EPR data had large uncertainty associated with it, due, in part, to small rubidium resonance signal and large background field variation. Nevertheless, the preliminary ^{129}Xe EPR shift sets a limit on the Rb-^{129}Xe enhancement factor.